J. Fluid Mech. (2011), *vol.* 667, *pp.* 403–425. © Cambridge University Press 2011
doi:10.1017/S0022112010004490

New bounds on the sedimentation velocity for hard, charged and adhesive hard-sphere colloids

W. TODD GILLELAND[1], SALVATORE TORQUATO[2] AND WILLIAM B. RUSSEL[1]†

[1]Department of Chemical Engineering, Department of Chemistry,
Princeton University, Princeton, NJ 08544, USA

[2]Department of Physics, Center for Theoretical Science, Princeton University, Princeton, NJ 08544, USA

(Received 6 February 2010; revised 18 July 2010; accepted 20 August 2010)

The sedimentation velocity of colloidal dispersions is known from experiment and theory at dilute concentrations to be quite sensitive to the interparticle potential with attractions/repulsions increasing/decreasing the rate significantly at intermediate volume fractions. Since the differences necessarily disappear at close packing, this implies a substantial maximum in the rate for attractions. This paper describes the derivation of a robust upper bound on the velocity that reflects these trends quantitatively and motivates wider application of a simple theory formulated for hard spheres. The treatment pertains to sedimentation velocities slow enough that Brownian motion sustains an equilibrium microstructure without large-scale inhomogeneities in density.

Key words: colloids, low-Reynolds-number flows

1. Introduction

Dispersions of submicron particles in water or organic liquids are essential to a wide range of technologies. Whether synthesized from small molecules or ground to the colloidal state from larger chunks, formulation and processing as a fluid dispersion is generally inevitable as dry powders of such small particles are unmanageable (Hunter 1987). Hence, the nature of the thermodynamic state and the mechanical properties of the dispersions as a function of the composition have long been the prime focus of the field. As with molecular fluids, transport properties of fluid dispersions of colloidal particles depend on the spatial distribution of the particles, as well as the driving forces causing the motion and the viscous stresses that result (van de Ven 1989; Pusey 1991; Russel *et al.* 1991). The transport coefficients that receive the most attention are the self and mutual diffusion coefficients, the sedimentation velocity and the shear viscosity for spherical particles in Newtonian fluids. The spatial distribution of particles in an equilibrium fluid phase is governed by the thermodynamics, i.e. the balance between thermal energy (kT) and interparticle potentials Φ that yields the lowest energy state. Since an external force F can perturb the equilibrium distribution significantly, we focus here on the weak force limit, i.e. $F \ll kT/a$ for spheres of radius a, for which the flow only slightly perturbs the microstructure and the response is linear. This distinguishes the phenomena from $aF/kT \gg 1$, i.e.

† Email address for correspondence: wbrussel@princeton.edu

non-Brownian (Nguyen & Ladd 2005), or $aF/kT \sim O(1)$ (Moncha-Jorda *et al.* 2010), in which the slowly decaying velocity field associated with individual settling particles can produce large-scale velocity and concentration fluctuations. In colloidal dispersions, thermodynamic interactions tend to suppress large-scale concentration fluctuations except in regions of the phase diagram where attractive interparticle potentials encourage phase separation.

The sedimentation velocity $U(\phi)$ of colloidal dispersions at finite volume fractions ϕ is widely recognized to depend strongly, both quantitatively and qualitatively, on the interparticle potential (Buscall *et al.* 1982; Jansen *et al.* 1986; de Kruif *et al.* 1987; Brady & Durlofsky 1988; Paulin & Ackerson 1990; Thies-Weesie *et al.* 1995). Though rarely exploited these days for diagnostic purposes, the fact that attractions increase the rate of settling, while repulsions decrease it, provides a clear signal of the character of the interactions. Of course, the practice of flocculating dispersions in order to accelerate the separation of solids from the liquid is a long-standing technology with polymeric flocculants that adsorb on and bridge between particles the most common additive, though depletion due to non-adsorbing polymers also occupies a niche market (Napper 1983; Fleer *et al.* 1993). For dispersions, in which the interactions are predominantly repulsive, the sedimentation velocity decreases monotonically with increasing volume fraction. For dispersions of hard spheres, the simplest repulsion, the behaviour is well characterized experimentally and, to some extent, theoretically. For charged spheres, the velocity is understood to be bounded from above by hard spheres and from below by the theoretical result for face-centred cubic arrays (Zick & Homsy 1982; Brady & Durlofsky 1988), which can be achieved with very strong or long-ranged potentials.

Aside from hard spheres and ordered arrays, fundamental understanding is limited to rigorous results for the dilute limit for spheres with model potentials captured in a general sense by an excluded volume of diameter s_o normalized on the sphere radius a and an adhesive attraction of dimensionless strength $1/\tau$. This generalized potential yields a pair correlation function $g(s)$ at dilute volume fractions $\phi \ll 1$ of $g(s) = \exp(-\Phi(s)/kT) = H(s - s_o) + \delta(s - s_o)/6\tau$ and a dilute limit of the form

$$U/U_o = 1 - (K_o - K_1/\tau)\phi + O(\phi^2), \tag{1.1}$$

with U_o the Stokes settling velocity for a sphere, K_o and K_1 accounting for hydrodynamic interactions via the method of reflections (Russel *et al.* 1991) and

$$H(s) = \begin{cases} 0 & s < 0, \\ 1 & s > 0, \end{cases} \quad \delta(s) = \frac{\mathrm{d}H}{\mathrm{d}s}. \tag{1.2}$$

This reduces to

$$U/U_o = 1 - 6.55\phi + O(\phi^2) \tag{1.3}$$

for hard spheres with $s_o = 2$ (Batchelor 1972),

$$U/U_o = 1 - \tfrac{3}{2}[\ln(\alpha/\ln(\alpha/\ln(\alpha/\ldots)))/a\kappa]^2\phi + O(\phi^2), \tag{1.4}$$

with $s_o = \ln(\alpha/\ln(\alpha/\ln(\alpha/\ldots)))/a\kappa$ and $\alpha = 4\pi\varepsilon\varepsilon_o\psi_s^2 a^2\kappa \exp(2a\kappa)/kT \gg 1$ for charged spheres with surface potential ψ_s and Debye screening length $1/\kappa$ ($ee_o =$ dielectric permittivity), and

$$U/U_o = 1 - (6.55 - 1.02/\tau)\phi + O(\phi^2). \tag{1.5}$$

for adhesive hard spheres.

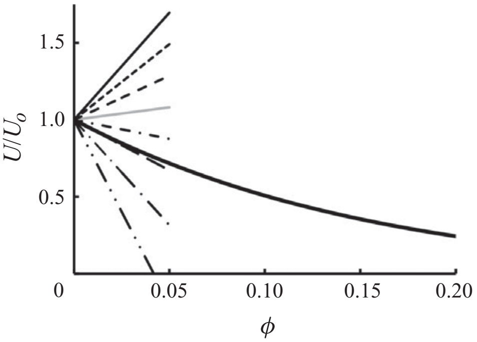

FIGURE 1. Dilute limit for dimensionless sedimentation velocity for charged ($s_o = 2$ (—), 3 (-··-), and 4 (-···-)) and adhesive hard spheres ($\tau = 0.250$ (-··-), 0.125 (—), 0.083 (–-), 0.062 (- - -) and 0.05 (—)) compared with the master curve (1.6) for hard spheres.

The only approximate theory recognizing both hydrodynamic interactions and the equilibrium microstructure of disordered dispersions was formulated by Brady & Durlofsky (1988), with pairwise additive hydrodynamics in the far-field approximation of Rotne–Prager. This leads to a simple approximation

$$U^{BD}/U_o = 1 - 5\phi - \frac{1}{5}\phi^2 + 3\phi \int_2^\infty h(s)s \, \mathrm{d}s, \tag{1.6}$$

where $h = g - 1$ is the total correlation function. Though applicable in general to the full range of interparticle potentials, this theory has not been evaluated or tested except for hard spheres. To illustrate the corresponding range of behaviours, we compare these dilute limits for charged and adhesive hard spheres with the master curve constructed from experimental data for hard spheres

$$U/U_o = (1 - \phi)^{5.4}/(1 + 1.15\phi) \tag{1.7}$$

in figure 1. Clearly, the dilute theories imply a remarkable sensitivity to the interparticle potential at finite concentrations, for which little is known quantitatively except that all should converge to the hard-sphere limit as the volume fraction approaches close packing.

To provide guidance on the behaviour at volume fractions beyond the dilute limit, we report here rigorous upper bounds on U for the range of interaction potentials described above. The bound is derived from an energy balance equating the rate of work $\dot{W}$ done by the gravitational force F_g with the rate of viscous dissipation $\dot{D}$ due to the sedimentation process, i.e.

$$\dot{W} = N F_g U = \dot{D} = V \langle \boldsymbol{\tau} : \boldsymbol{\tau}/2\mu \rangle \tag{1.8}$$

for a volume V containing N particles (Luke 1992, 1993). By constructing approximations for the stress fields $\boldsymbol{\tau}$ to estimate the rate of dissipation, which is minimized by the exact fields, one can construct, in principle, increasingly accurate bounds on the sedimentation velocity as proposed by Torquato & Beasley (1987) and Torquato (2002). Here we take only the first step, employing the single-particle ‘trial’ velocity fields, i.e. the first step in the method of reflections, with accurate approximations for the volume fraction-dependent pair distribution function to construct a two-point bound. The beauty of the approach, which improves on the earlier work by Luke, is that even a crude approximation for the hydrodynamics yields considerable quantitative information about sedimentation, because of the dominant role of 'backflow' identified by Batchelor (1972) in his dilute theory.

2. Bulk properties from energy dissipation

The key to developing upper and lower bounds on the macroscopic properties of dispersions is their relationship to a microscopic energy balance. The energy conserved or dissipated is directly related to the bulk property and the macroscopic boundary conditions. For example, the dissipation of energy by simple shear flow is characterized by the macroscopic viscosity and rate of strain. In a similar manner, the sedimentation velocity, fluid permeability, electrical conductivity, nuclear magnetic resonance decay rate, elastic moduli and other transport properties can be represented rigorously in terms of macroscopic energy relations (Torquato 2002). Once a relation is developed between the transport property of interest and the overall energy balance, statistical mechanics can be invoked to connect the microscopic and macroscopic formulations. The ensemble average of the volume integral of the exact microscopic energy dissipation equals that of the bulk system. From this, integral bounds are developed and evaluated from estimates of the microscopic dissipation derived from approximate trial velocity fields.

Since particle trajectories are not known *a priori* in a flowing suspension, trial fields that match exactly the motion of the particle cannot be constructed. To derive an applicable upper bound, we synthesize a new proof, drawing from Torquato (2002) the concept of bounding the minimum complementary energy in terms of the deviatoric stress and the minimum principle based on the rate of strain (Luke 1992, 1993). The new proof specifies the total force and torque on the particle instead of point-wise velocities or stresses, providing an approach amenable to flowing suspensions. The resulting trial stress field $\hat{\boldsymbol{\sigma}}$ then differs from the unknown exact solution $\boldsymbol{\sigma}$ by the variational field $\boldsymbol{\sigma}'$. The trial field must satisfy the Stokes equation with prescribed forces and torques on the particles,

$$\left.\begin{aligned} &\nabla\cdot\hat{\boldsymbol{\sigma}} = 0, \quad \nabla\cdot\hat{\boldsymbol{u}} = 0, \quad \text{in } V_f \\ &\int_{A_i} \hat{\boldsymbol{\sigma}}\cdot\boldsymbol{n}\,\mathrm{d}^2\boldsymbol{x} = \boldsymbol{F}, \quad \int_{A_i} (\boldsymbol{x}-\boldsymbol{x}_i)\times\hat{\boldsymbol{\sigma}}\cdot\boldsymbol{n}\,\mathrm{d}^2\boldsymbol{x} = 0. \end{aligned}\right\} \tag{2.1}$$

This formulation requires the stress and velocity fields to be divergence-free but imposes no constraint on the velocity at the particle surfaces as long as the total force and torque conditions are met.

While proving the minimum principle based on the full stress $\boldsymbol{\sigma}$ would seem preferable, an exact solution for the pressure component of the stress is unknown. Thus, cross-terms between $\boldsymbol{\sigma}$ and $\hat{\boldsymbol{\sigma}} \equiv \boldsymbol{\sigma}[\hat{\boldsymbol{u}}]$, with [ ] indicating a functional dependence, cannot be eliminated. In contrast, one can prove the traceless form of the minimum principle,

$$\left\langle \frac{1}{2\mu}\boldsymbol{\tau}[\boldsymbol{u}] : \boldsymbol{\tau}[\boldsymbol{u}] \right\rangle \leqslant \left\langle \frac{1}{2\mu}\boldsymbol{\tau}[\hat{\boldsymbol{u}}] : \boldsymbol{\tau}[\hat{\boldsymbol{u}}] \right\rangle, \tag{2.2}$$

with the deviatoric stress $\boldsymbol{\tau} = \boldsymbol{\sigma} - (1/3)\mathrm{tr}(\boldsymbol{\sigma})\boldsymbol{\delta}$. The use of (2.2) with Torquato's constraints and trial fields yields a lower bound on the sedimentation velocity, but substitution of our traceless stress field transforms that into an upper bound on the sedimentation velocity.

To prove the minimum principle (2.2), we expand the product $\hat{\boldsymbol{\tau}} : \hat{\boldsymbol{\tau}}$ in terms of the exact and variational fields $\boldsymbol{\tau}$ and $\boldsymbol{\tau}'$ as

$$\left\langle \frac{1}{2\mu}\boldsymbol{\tau}\,[\hat{\boldsymbol{u}}] : \boldsymbol{\tau}\,[\hat{\boldsymbol{u}}] \right\rangle = \left\langle \frac{1}{2\mu}\boldsymbol{\tau} : \boldsymbol{\tau} \right\rangle + \left\langle \frac{1}{2\mu}\boldsymbol{\tau}' : \boldsymbol{\tau}' \right\rangle + 2\left\langle \frac{1}{2\mu}\boldsymbol{\tau} : \boldsymbol{\tau}' \right\rangle. \tag{2.3}$$

The exact deviatoric stress depends on the strain rate $\boldsymbol{\tau} = 2\mu\boldsymbol{e}$, so that

$$\frac{1}{2\mu}\boldsymbol{\tau} = \boldsymbol{e} = \frac{1}{2}(\nabla\boldsymbol{u} + (\nabla\boldsymbol{u})^{\mathrm{T}}). \tag{2.4}$$

Since

$$\boldsymbol{e} : p'\boldsymbol{\delta} = p'\boldsymbol{e} : \boldsymbol{\delta} = (\nabla\boldsymbol{\cdot}\boldsymbol{u})p' = 0, \tag{2.5}$$

the cross-term can be written as

$$\begin{aligned}\left\langle \frac{1}{2\mu}\boldsymbol{\tau} : \boldsymbol{\tau}' \right\rangle &= \langle \boldsymbol{e} : \boldsymbol{\tau}' \rangle = \langle \boldsymbol{e} : (\boldsymbol{\tau}' + p'\boldsymbol{\delta}) \rangle = \langle \boldsymbol{e} : \boldsymbol{\sigma}' \rangle \\ &= \left\langle \boldsymbol{\sigma}' : \frac{1}{2}(\nabla\boldsymbol{u} + (\nabla\boldsymbol{u})^{\mathrm{T}}) \right\rangle = \langle \sigma' : \nabla\boldsymbol{u} \rangle. \end{aligned} \tag{2.6}$$

With the chain rule and the momentum equation (2.1),

$$\nabla\boldsymbol{\cdot}(\boldsymbol{\sigma}'\boldsymbol{\cdot}\boldsymbol{u}) = \boldsymbol{u}\boldsymbol{\cdot}(\nabla\boldsymbol{\cdot}\boldsymbol{\sigma}') + \boldsymbol{\sigma}' : \nabla\boldsymbol{u} = \boldsymbol{\sigma}' : \nabla\boldsymbol{u}, \tag{2.7}$$

and the ensemble average expressed as a volume integral, the cross-term becomes

$$\begin{aligned}\left\langle \frac{1}{2\mu}\boldsymbol{\tau} : \boldsymbol{\tau}' \right\rangle &= \langle \nabla\boldsymbol{\cdot}(\boldsymbol{\sigma}'\boldsymbol{\cdot}\boldsymbol{u}) \rangle = \frac{1}{V}\int_V \nabla\boldsymbol{\cdot}(\boldsymbol{\sigma}'\boldsymbol{\cdot}\boldsymbol{u})\mathrm{d}V \\ &= \sum_{l=1}^{N} \frac{1}{V}\oint_{A_l} \boldsymbol{n}\boldsymbol{\cdot}(\boldsymbol{\sigma}'\boldsymbol{\cdot}\boldsymbol{u})\mathrm{d}S + \frac{1}{V}\oint_{A} \boldsymbol{n}\boldsymbol{\cdot}(\boldsymbol{\sigma}'\boldsymbol{\cdot}\boldsymbol{u})\mathrm{d}S \equiv E_1 + E_2. \end{aligned} \tag{2.8}$$

Note that the divergence theorem casts the integral onto the surfaces of the particles A_i and the solid surface of the container A on which $\boldsymbol{u} = 0$, so that $E_2 = 0$.

The constraints (2.1) on the trial field, together with the solid body translation and rotation of the actual field, now serve to reduce to zero the integrals over all the particle surfaces, i.e.

$$\begin{aligned} E_1 &= \sum_{i=1}^{N} \frac{1}{V}\oint_{A_i} \boldsymbol{u}\boldsymbol{\cdot}\boldsymbol{\sigma}'\boldsymbol{\cdot}\boldsymbol{n}\,\mathrm{d}S \\ &= \sum_{i=1}^{N} \frac{1}{V}\oint_{A_i} \{\boldsymbol{U}_i\boldsymbol{\cdot}(\boldsymbol{\sigma}\,[\hat{\boldsymbol{u}}] - \boldsymbol{\sigma}\,[\boldsymbol{u}]) + (\boldsymbol{\Omega}_i \times \boldsymbol{r})\boldsymbol{\cdot}(\boldsymbol{\sigma}\,[\hat{\boldsymbol{u}}] - \boldsymbol{\sigma}\,[\boldsymbol{u}])\}\boldsymbol{\cdot}\boldsymbol{n}\,\mathrm{d}S \end{aligned} \tag{2.9}$$

Since $\boldsymbol{U}_i$ is constant and the forces for the trial and exact solution match so that $\boldsymbol{F}[\hat{\boldsymbol{u}}] - \boldsymbol{F}[\boldsymbol{u}] = 0$, the first term vanishes. By transposing the cross-product to identify the torque and recognizing that $\boldsymbol{\Omega}_i$ is constant and the torques for the trial and exact solution are both zero, the second term integrates to zero, so that

$$\begin{aligned}\oint_{A_i} (\boldsymbol{\Omega} \times \boldsymbol{r})\boldsymbol{\cdot}(\boldsymbol{\sigma}\,[\hat{\boldsymbol{u}}] - \boldsymbol{\sigma}\,[\boldsymbol{u}])\boldsymbol{\cdot}\boldsymbol{n}\,\mathrm{d}S &= \oint_{A_i} \boldsymbol{\Omega}\boldsymbol{\cdot}\{\boldsymbol{r} \times (\boldsymbol{\sigma}\,[\hat{\boldsymbol{u}}] - \boldsymbol{\sigma}\,[\boldsymbol{u}])\boldsymbol{\cdot}\boldsymbol{n}\}\mathrm{d}S \\ &= \boldsymbol{\Omega}_i\boldsymbol{\cdot}(\boldsymbol{T}\,[\hat{\boldsymbol{u}}] - \boldsymbol{T}\,[\boldsymbol{u}]) = 0. \end{aligned} \tag{2.10}$$

Thus, both parts of the first integral E_1 vanish.

With these results the viscous dissipation expressed in terms of the traceless stress reduces to a Pythagorean equation

$$\left\langle \frac{1}{2\mu}\hat{\boldsymbol{\tau}} : \hat{\boldsymbol{\tau}} \right\rangle = \left\langle \frac{1}{2\mu}\boldsymbol{\tau} : \boldsymbol{\tau} \right\rangle + \left\langle \frac{1}{2\mu}\boldsymbol{\tau}' : \boldsymbol{\tau}' \right\rangle \geqslant \left\langle \frac{1}{2\mu}\boldsymbol{\tau} : \boldsymbol{\tau} \right\rangle, \tag{2.11}$$

in which the positive dissipation from the variational stress field $\boldsymbol{\tau}'$ proves the minimum principle in (2.2) for trial stress fields that satisfy the constraints in (2.1).

2.1. *Mean sedimentation velocity and trial fields*

To relate the sedimentation velocity of a monodisperse suspension to the viscous dissipation, we simply require the rate of work performed by gravity,

$$\dot{W} = \sum_{i=1}^{N} \boldsymbol{U}_i \cdot \boldsymbol{F} \equiv nV\boldsymbol{F}\boldsymbol{U}, \tag{2.12}$$

with the mean sedimentation velocity U and $n = N/V$ the number density of particles, to be equal to the rate of viscous dissipation, and less than the trial estimate expressed as an ensemble average at a point, which yields an upper bound on the sedimentation velocity as

$$nUF = \left\langle \frac{1}{2\mu}\boldsymbol{\tau}:\boldsymbol{\tau} \right\rangle \leqslant \left\langle \frac{1}{2\mu}\boldsymbol{\tau}':\boldsymbol{\tau}' \right\rangle. \tag{2.13}$$

To evaluate (2.13) as a two-point upper bound requires three steps: construction of a trial velocity field satisfying the requisite constraints (2.1), formulation of the local dissipation in terms of pair statistics for the particles, and integration to create the bound. A final physical constraint is necessary to prevent non-convergent integrals. This is achieved by constraining the sum of velocities into and out of any volume or across any plane to be zero or equivalently requiring the ensemble average of the velocity to be zero at every point. This is fully equivalent to the renormalizations constructed by Batchelor (1972) and O'Brien (1979).

The ensemble average is over all possible points in the volume, within and outside of particles, with a viscosity and strain appropriate to the test point. Partitioning the ensemble average to distinguish the strain fields $\hat{\boldsymbol{e}}_p$ inside a particle and $\hat{\boldsymbol{e}}_f$ in the fluid yields

$$\langle 2\mu\hat{\boldsymbol{e}} : \hat{\boldsymbol{e}} \rangle = \langle 2\mu\hat{\boldsymbol{e}}_f : \hat{\boldsymbol{e}}_f I^f \rangle + \langle 2\mu_p\hat{\boldsymbol{e}}_p : \hat{\boldsymbol{e}}_p I^p \rangle, \tag{2.14}$$

with binary phase indicator functions, I^p and I^f, for the particle and fluid phases defined by

$$\left.\begin{aligned} I^f(\boldsymbol{x}) &= \prod_{i=1}^{N} H(|\boldsymbol{x}-\boldsymbol{r}_i|/a) \quad \text{with} \quad \left\langle I^f(\boldsymbol{x}) \right\rangle = 1-\phi, \\ I^p(\boldsymbol{x}) &= \sum_{i=1}^{N} (1 - H(|\boldsymbol{x}-\boldsymbol{r}_i|/a)) \quad \text{with} \quad \langle I^p(\boldsymbol{x}) \rangle = \phi, \end{aligned}\right\} \tag{2.15}$$

and $H(|\boldsymbol{x} - \boldsymbol{r}_i|/a)$ the Heaviside step function. Since the viscous dissipation is identically zero within elastic or hard particles, the overall dissipation becomes

$$\langle 2\mu\hat{\boldsymbol{e}} : \hat{\boldsymbol{e}} \rangle = \left\langle 2\mu\hat{\boldsymbol{e}}_f : \hat{\boldsymbol{e}}_f I^f \right\rangle. \tag{2.16}$$

This ensemble average of the inner product of two trial strain fields multiplied by the fluid phase indicator I^f requires information on three locations, the sampling point and the centres of the two particles generating the strain fields. Evaluation

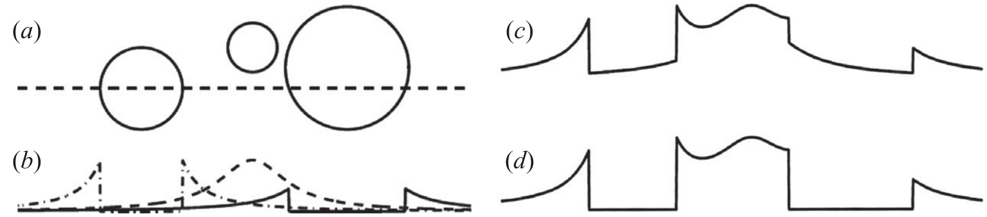

FIGURE 2. Schematic of trial strain field: (*a*) spheres of different sizes have centres that lie on a horizontal plane containing a dashed line that passes through the centre of the leftmost sphere. (*b*) The magnitude of the lowest-order term in the disturbance field generated by each individual sphere along the dashed line. (*c*) The trial strain field is the sum of the individual fields and, therefore, is non-zero within the spheres. (*d*) The product of the trail strain field and the phase indicator function I_f makes the strain zero within each particle. The approximation of $I_f = 0$ loosens the upper bound by counting dissipation in the volume occupied by the particles.

of this quantity results in a three-point bound as demonstrated previously for hard spheres (Beasley & Torquato 1989).

Here, to obtain a more tractable computation, we reduce the order of the bound by noting that $I^f \leqslant 1$, so that approximating $I^f = 1$ retains an upper bound as

$$nUF = \left\langle \frac{1}{2\mu}\boldsymbol{\tau} : \boldsymbol{\tau} \right\rangle \leqslant \langle 2\mu \hat{\boldsymbol{e}}_f : \hat{\boldsymbol{e}}_f \rangle. \tag{2.17}$$

The subscript indicates that sampling points within either of the two particles still yield no dissipation.

For simplicity we take the trial velocity field $\hat{\boldsymbol{u}}$ for a particular configuration of particles as the sum of the single particle velocity fields $\boldsymbol{u}_o$ outside of the source particle, minus the mean trial velocity,

$$\hat{\boldsymbol{u}}(\boldsymbol{x}) = \sum_{i=1}^{N} \boldsymbol{u}_o(\boldsymbol{x}-\boldsymbol{r}_i)\, H(|\boldsymbol{x}-\boldsymbol{r}_i|/1) - n\int \boldsymbol{u}_o(\boldsymbol{x}-\boldsymbol{r})\, H(|\boldsymbol{x}-\boldsymbol{r}_i|/a)\,\mathrm{d}\boldsymbol{r}_i \tag{2.18}$$

with

$$\boldsymbol{u}_o(\boldsymbol{r}) = \boldsymbol{F}\boldsymbol{\cdot}\left(1+\frac{a^2}{6}\nabla^2\right)\boldsymbol{I}(\boldsymbol{r}) \quad \text{with} \quad \boldsymbol{I}(\boldsymbol{r}) = \frac{1}{8\pi\mu r}\left(\delta + \frac{\boldsymbol{rr}}{r^2}\right). \tag{2.19}$$

The single particle $\boldsymbol{e}_o$ and trial $\hat{\boldsymbol{e}}_f$ strain fields follow as

$$\left.\begin{aligned} \boldsymbol{e_o}(\boldsymbol{r}) &= \frac{1}{2}(\nabla\boldsymbol{u}_o(\boldsymbol{r}) + (\nabla\boldsymbol{u}_o(\boldsymbol{r}))^{\mathrm{T}}) \\ &= -\frac{\boldsymbol{F}}{8\pi\mu r^2}\left\{3\frac{\boldsymbol{rrr}}{r^3}\left(1-\frac{5a^2}{3r^2}\right) + \frac{\boldsymbol{\delta r}+\boldsymbol{r\delta}+(\boldsymbol{\delta r})^t}{r}\frac{a^2}{r^2} - \frac{\boldsymbol{r\delta}}{r}\right\}, \\ \hat{\boldsymbol{e}}(\boldsymbol{x}) &= \sum_{i=1}^{N}\boldsymbol{e}_o(\boldsymbol{x}-\boldsymbol{r}_i)\,H(|\boldsymbol{x}-\boldsymbol{r}_i|/a) - n\int \boldsymbol{e}_o(\boldsymbol{x}-\boldsymbol{r})\,H(|\boldsymbol{x}-\boldsymbol{r}_i|/a)\,\mathrm{d}^3\boldsymbol{r}. \end{aligned}\right\} \tag{2.20}$$

This amounts to the first term in a method of reflections in the standard terminology for hydrodynamic interactions among particles. The consequences of this trial strain field, which satisfies the constraints prescribed above, are depicted in figure 2, displaying the superimposition of single particle fields (2.18) and discounting the fluid phase indicator function (2.15).

2.2. *Simplification of the two-point bound*

The technique developed by Beasley & Torquato (1989) represents the trial fields in terms of scalar Legendre polynomials to reduce the six-dimensional integral required by the ensemble average to three dimensions. The first step is to separate the scalar decay in the disturbance fields $\boldsymbol{e}_o$ from the angular dependence represented by tensorial products of the unit normal $\boldsymbol{n}$ and the applied force $\boldsymbol{F}$ as

$$\boldsymbol{e}_o(\boldsymbol{r}) = -\frac{a^2}{8\pi\mu r^4}\left(\boldsymbol{nF} + \boldsymbol{Fn} - \frac{2}{3}\boldsymbol{n}\cdot\boldsymbol{F}\boldsymbol{\delta}\right) - \frac{3}{8\pi\mu r^2}\left(1 - \frac{5a^2}{3r^2}\right)\boldsymbol{n}\cdot\boldsymbol{F}\left(\boldsymbol{nn} - \frac{1}{3}\boldsymbol{\delta}\right). \tag{2.21}$$

Aligning the z-axis of the coordinate frame with the applied force as $\boldsymbol{F} = F\boldsymbol{\delta}_z$, converting to spherical coordinates with $f = F/8\pi\mu a^2$, $a(r) = -a^2/r^4$, and $b(r) = -3(1 - 5a^2/3r^2)/r^2$, and expressing the double inner product of disturbance fields $e_1(\boldsymbol{r}_1) : e_1(\boldsymbol{r}_2)$ in terms of Legendre polynomials $P_n(x)$ eventually leads to

$$\begin{aligned} f^{-2}\boldsymbol{e}_o(\boldsymbol{r}_1) : \boldsymbol{e}_o(\boldsymbol{r}_2) = {} & 2a(r_1)\,a(r_2)\left(\boldsymbol{n}_1\cdot\boldsymbol{n}_2 + \tfrac{1}{3}P_1(x_1)\,P_1(x_1)\right) \\ & + \tfrac{2}{3}a(r_1)\,b(r_2)\,(\boldsymbol{n}_1\cdot\boldsymbol{n}_2\,(P_0(x_2) + 2P_2(x_2)) - P_1(x_1)\,P_1(x_2)) \\ & + \tfrac{2}{3}a(r_2)\,b(r_1)\,(\boldsymbol{n}_1\cdot\boldsymbol{n}_2\,(P_0(x_1) + 2P_2(x_1)) - P_1(x_1)\,P_1(x_2)) \\ & + b(r_1)\,b(r_2)\left(\boldsymbol{n}_1\cdot\boldsymbol{n}_2 P_1(x_1)\,P_1(x_2) - \tfrac{1}{3}P_1(x_1)\,P_1(x_2)\right). \end{aligned} \tag{2.22}$$

Expanding the weighting functions, represented as an arbitrary function of two vectors, yields

$$\chi(\boldsymbol{r}_1)\,\chi(\boldsymbol{r}_2)\,h(r_{12}) = \chi(\boldsymbol{r}_1)\,\chi(\boldsymbol{r}_2)\,[g(r_{12}) - 1] \equiv k(\boldsymbol{r}_1, \boldsymbol{r}_2) = \sum_{n=0}^{\infty} K_n(r_1, r_2)\,P_n(\boldsymbol{n}_1\cdot\boldsymbol{n}_2), \tag{2.23}$$

with $r_1 = |\boldsymbol{r}_1|$ and $\boldsymbol{n}_1 = \boldsymbol{r}_1/r_1$ and the expansion coefficients

$$K_n(r_1, r_2) = \frac{2n+1}{2}\int_{-1}^{+1} k(\boldsymbol{r}_1, \boldsymbol{r}_2)P_n(\boldsymbol{n}_1\cdot\boldsymbol{n}_2)\,d(\boldsymbol{n}_1\cdot\boldsymbol{n}_2). \tag{2.24}$$

The total integral for the dissipation

$$I = \iint k(\boldsymbol{r}_1, \boldsymbol{r}_2)\,\boldsymbol{e}_1(\boldsymbol{r}_1) : \boldsymbol{e}_1(\boldsymbol{r}_2)\,\mathrm{d}\boldsymbol{r}_1\,\mathrm{d}\boldsymbol{r}_2 \tag{2.25}$$

can be reorganized by setting $\boldsymbol{r}_1 = r_i\hat{\boldsymbol{n}}_i$, with $\mathrm{d}\hat{\boldsymbol{n}}_i$ a differential element of solid angle, and inserting the expansion for the distribution function to obtain

$$I = \int_0^{\infty}\int_0^{\infty}\sum_{i=0}^{\infty} K_i(r_1, r_2)\,r_2^2\,\mathrm{d}r_2 r_1^2\,\mathrm{d}r_1. \tag{2.26}$$

To evaluate the last pair of angular integrals over $\mathrm{d}\hat{\boldsymbol{n}}_1\,\mathrm{d}\hat{\boldsymbol{n}}_2$, we apply the addition theorem

$$\begin{aligned} P_n(\boldsymbol{n}_1\cdot\boldsymbol{n}_2) = {} & P_n(\cos\theta_1)\,P_n(\cos\theta_2) \\ & + 2\sum_{m=1}^{n}\frac{(n-m)!}{(n+m)!}P_\ell^m(\cos\theta_1)\,P_n^m(\cos\theta_2)\cos(m(\phi_1 - \phi_2)), \end{aligned} \tag{2.27}$$

and the Legendre polynomial representation of the angular components:

$$
\begin{aligned}
&\sum_{i=0}^{\infty} F_i\left(r_1, r_2\right) \iint P_i\left(\boldsymbol{n}_1 \cdot \boldsymbol{n}_2\right) \boldsymbol{e}_1\left(\boldsymbol{r}_1\right) : \boldsymbol{e}_1\left(\boldsymbol{r}_2\right) \mathrm{d}\boldsymbol{n}_1 \mathrm{d}\boldsymbol{n}_2 \\
&\quad = f^2 \sum_{\ell=0}^{\infty} K_i\left(r_1, r_2\right) \iint \left[P_i\left(\cos\theta_1\right) P_i\left(\cos\theta_2\right)\right. \\
&\quad \left. + 2\sum_{m=1}^{i} \frac{(i-m)!}{(i+m)!} P_i^m\left(\cos\theta_2\right) \cos\left(m\left(\phi_1-\phi_2\right)\right)\right] \\
&\quad \times \left\{ 2a\left(r_1\right) a\left(r_2\right) \left[\boldsymbol{n}_1 \cdot \boldsymbol{n}_2 + \frac{1}{3} P_1\left(\cos\theta_1\right) P_1\left(\cos\theta_2\right)\right]\right. \\
&\quad + \frac{2}{3} a\left(r_1\right) b\left(r_2\right) \left[\boldsymbol{n}_1 \cdot \boldsymbol{n}_2 \left(P_0\left(\cos\theta_2\right) + 2P_2\left(\cos\theta_2\right)\right) - P_1\left(\cos\theta_1\right) P_1\left(\cos\theta_2\right)\right] \\
&\quad + \frac{2}{3} b\left(r_1\right) a\left(r_2\right) \left[\boldsymbol{n}_1 \cdot \boldsymbol{n}_2 \left(P_0\left(\cos\theta_1\right) + 2P_2\left(\cos\theta_1\right)\right) - P_1\left(\cos\theta_1\right) P_1\left(\cos\theta_2\right)\right] \\
&\quad \left. + b\left(r_1\right) b\left(r_2\right) \left[\left(\boldsymbol{n}_1 \cdot \boldsymbol{n}_2\right)^2 P_1\left(\cos\theta_1\right) P_1\left(\cos\theta_2\right) - \frac{1}{3} P_1\left(\cos\theta_1\right) P_1\left(\cos\theta_2\right)\right]\right\} \mathrm{d}\boldsymbol{n}_1\, \mathrm{d}\boldsymbol{n}_2.
\end{aligned}
\tag{2.28}
$$

To evaluate K_n requires conversion of $\mathrm{d}\boldsymbol{n}_1 \cdot \boldsymbol{n}_2$ to $\mathrm{d}r_{12}$ by expressing the distance as $r_{12}^2 = \boldsymbol{r}_1 \cdot \boldsymbol{r}_1 + \boldsymbol{r}_2 \cdot \boldsymbol{r}_2 - 2\boldsymbol{r}_1 \cdot \boldsymbol{r}_{22} = r_1^2 + r_2^2 - 2r_1 r_2 \boldsymbol{n}_1 \cdot \boldsymbol{n}$ so that $\boldsymbol{n}_1 \cdot \boldsymbol{n}_2 = (r_1^2 + r_2^2 - r_{12}^2)/2r_1 r_2$ and $\mathrm{d}\left(\boldsymbol{n}_1 \cdot \boldsymbol{n}_2\right) = -r_{12}/r_1 r_2\, \mathrm{d}r_{12}$. The limits of the integration follow as $r_{12} = |r_1 + r_2|$, corresponding to $\boldsymbol{n}_1 \cdot \boldsymbol{n}_2 = -1$, and $r_{12} = |r_1 - r_2|$, corresponding to $\boldsymbol{n}_1 \cdot \boldsymbol{n}_2 = +1$. Finally, the integral in terms of $\mathrm{d}r_{12}$ is

$$
\begin{aligned}
I = \frac{f^2}{60\mu^2} \int_0^{\infty} \chi\left(r_1\right) \int_0^{\infty} \chi\left(r_2\right) \int_{|r_1 - r_2|}^{r_1 + r_2} \frac{r_{12}}{r_1 r_2} h\left(r_{12}\right) \\
\times \left\{ \frac{6}{r_1^2 r_2^2} P_1(\Delta r^2) + b\left(r_1\right) b\left(r_2\right) P_3(\Delta r^2) \right\} r_1^2 r_2^2\, \mathrm{d}r_1\, \mathrm{d}r_2\, \mathrm{d}r_{12}
\end{aligned}
\tag{2.29}
$$

with $\Delta r^2 \equiv (r_1^2 + r_2^2 - r_{12}^2)/2r_1 r_2$. The two-particle integral then can be simplified to a scalar integral in one dimension over the pair correlation function:

$$
I = \frac{f^2}{3\mu^2} \left[\int_2^{\infty} s h(s)\, \mathrm{d}s - \int_0^2 \left(s^2 - \frac{1}{4} s^3\right) \mathrm{d}s\right] = \frac{f^2}{9\mu^2} \left[-5 + 3\int_2^{\infty} s h(s)\, \mathrm{d}s\right]. \tag{2.30}
$$

The second integral, for $0 \leqslant s = r/a \leqslant 2$, where $h(x) = -1$, accounts for the hard sphere excluded volume.

With the value of the integral I, the two-point upper bound on sedimentation takes the form

$$
U/U_0 \leqslant 1 - 5\phi + 3\phi \int_2^{\infty} s h(s)\, \mathrm{d}s, \tag{2.31}
$$

with -5ϕ corresponding to the contribution from ‘backflow’ calculated by Batchelor through renormalization of a non-convergent integral (Batchelor 1972). Here the same result is reached through conservation of volume enforced by normalizing the trial fields to zero mean in (2.18) and (2.20). Note that this upper bound corresponds to $U^{BD}/U_o + \phi^2/5$, so the approximation of Brady & Durlofsky (1.6) satisfies the upper bound for all volume fractions and all interparticle potentials, a point that has not been exploited.

3. Pair correlation functions for model colloids

In colloidal suspensions, one encounters a broad range of interparticle potentials, depending on the composition and size of the particles and the nature and composition of the intervening fluid. Potentials vary from the simple repulsive or adhesive contact of hard or sticky spheres through electrostatic repulsions that can extend to separations of a micron. When the solvent and any solutes equilibrate thermodynamically much faster than the particles, their effects can be lumped into a potential of mean force that is employed as the interparticle potential. If not, the dispersion must be treated as a multi-component mixture. Here we consider three representative pair potentials to demonstrate the sensitivity to the microstructure of the upper bound on the sedimentation velocity. The equilibrium pair correlation function $g(r)$, which follows from the potential, characterizes the microstructure of the dispersion. In a disordered fluid phase, particles become uncorrelated at large separations, so the distribution function asymptotically approaches unity.

Here we seek the pair distribution function for hard, charged and adhesive hard spheres from infinite dilution to as high a volume fraction as possible. The total correlation function h can be calculated through the Ornstein–Zernike equation (Hansen & McDonald 1986),

$$h(r_{12}) = c(r_{12}) + n\int c(r_{13})h(r_{13})\,\mathrm{d}\boldsymbol{r}_3, \tag{3.1}$$

which defines the direct correlation function $c(r)$. Applying a Fourier transform produces

$$\hat{H}(\boldsymbol{k}) = \hat{C}(\boldsymbol{k}) + n\hat{H}(\boldsymbol{k})\hat{C}(\boldsymbol{k}), \tag{3.2}$$

where $\hat{H}$ and $\hat{C}$ are the Fourier transforms of h and c, respectively. This provides a basis for calculating pair correlations in real space through closure approximations for the direct correlation function. The Percus–Yevick (PY) approximation consists of

$$c\,(r) = g\,(r)\,[1 - \exp(\Phi(r)/kT)], \tag{3.3}$$

while the hypernetted chain approximation follows from

$$c\,(r) = -\Phi\,(r)\,/kT + h\,(r) - \ln\,[h\,(r) + 1]. \tag{3.4}$$

The modified hypernetted chain approximation adds a bridge function to the right-hand side that provides an additional short-range repulsion adjusted to reproduce the accurate equation of state for hard spheres. For charged spheres the separations are simply rescaled with the effective hard-sphere diameter $d_{eff}/2a > 1$.

For hard spheres

$$\frac{\Phi}{kT}(s) = \begin{cases} \infty & s < 2 \\ 0 & 2 < s \end{cases} \tag{3.5}$$

the PY solution for $g(r)$ is available analytically (Baxter 1970) or through a numerical fast Fourier transform of the simpler analytical static structure factor. Verlet & Weis' (1972) (VW) correction to the PY solution provides a form that matches empirically results from simulations. Both approaches are valid for the equilibrium liquid phase from infinite dilution to $\phi = 0.494$, beyond which a face-centred cubic crystal emerges at $\phi = 0.545$. However, a metastable fluid phase often persists until random close packing at $\phi = 0.64$.

Since both the PY and VW results will err near random close packing, we also performed Monte Carlo (MC) simulations, adopting the general technique of

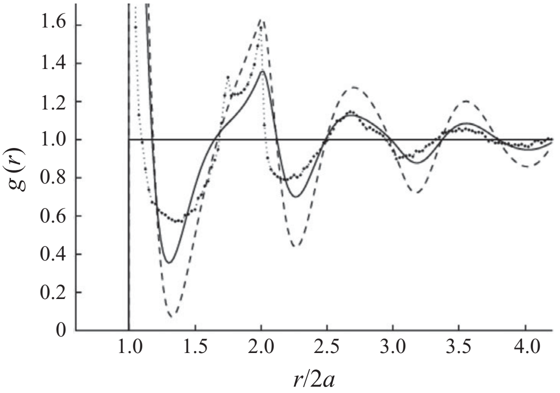

FIGURE 3. Comparison of distribution functions from Percus–Yevick $g(r)$ without (- - -) and with (—) the VW correction with MC (········) results at $\phi = 0.60$.

Metropolis sampling (Allen & Tildesley 1987) with several enhancements at the highest densities. Initial configurations were generated by random sequential addition followed by particle growth augmented by vector growth displacement (Clarke & Wiley 1987) as implemented previously (Rintoul & Torquato 1996). To the latter we added a damping factor to the amplitude of the move or half moves when the full displacement generated an overlap. During the simulation, local bond order, as indicative of face-centred cubic structure, was monitored through calculation of Q_6 (Steinhardt *et al.* 1983; Rintoul & Torquato 1998),

$$Q_6 = \left(\frac{4\pi}{13} \sum_{m=-6}^{6} \left| \bar{Q}_{6m} \right|^2 \right)^{1/2} \quad \text{with} \quad \bar{Q}_{6m} = \frac{1}{\boldsymbol{n}_b} \sum_{i-1}^{\boldsymbol{n}_b} Y_{6m} \left(\theta \left(\boldsymbol{r}_i \right), \phi \left(\boldsymbol{r}_i \right) \right), \tag{3.6}$$

where Y_{lm} are the spherical harmonics, $N_b =$ number of bonds, θ, ϕ and $\boldsymbol{r}_i$ are the bond angles and bond vector. Simulation boxes of 18 particle diameters on a side contained 600–7500 particles, depending on the volume fraction. The most meaningful measure of order proved to be $Q_6\sqrt{N_b}$, which is 2 for a face-centred cubic crystal, the equilibrium state for hard spheres at $\phi > 0.494$. For our simulations, $1 < Q_6\sqrt{N_b} < 1.4$ and changed little for simulations at $0.25 < \phi < 0.625$, which indicated a fluid microstructure. Only at the very highest volume fraction did this measure creep upward during the simulation (Gilleland 2004). Figure 3 demonstrates the correspondence before and after correction with MC results at the extreme volume fraction of $\phi = 0.60$. The split peaks most noticeable in MC data indicate a tendency towards the face-centred cubic structure.

For spheres bearing Q charges, modelled by a Yukawa potential with a hard core (Thies-Weesie *et al.* 1995),

$$\frac{\Phi}{kT}(s) = \infty H(2 - s) + \frac{\ell_b}{a} \frac{Q^2 \exp\left[-a\kappa (s - 2)\right]}{(1 + a\kappa)^2 s}, \tag{3.7}$$

the Debye screening factor κ increases with volume fraction from that for the initial solution κ_o as

$$(a\kappa)^2 = (a\kappa_o)^2 + \frac{\ell_b}{a} \frac{3\phi}{1 - \phi} Q, \tag{3.8}$$

due to the volume occupied by particles and the counterions accompanying the particle charge. Note that the potential is specified by three dimensionless parameters, a/λ_b

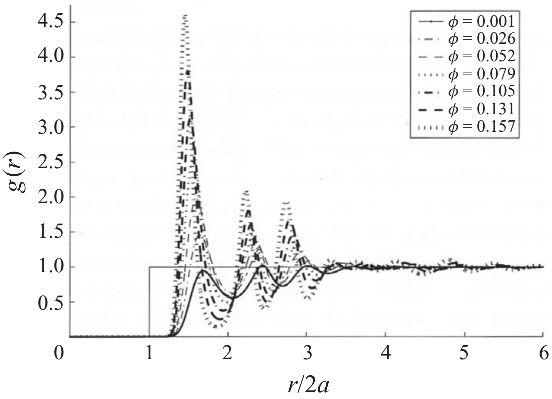

FIGURE 4. Distribution functions for charged spheres with $a/\lambda_b = 12.6$, $Q = 75$ and $a\kappa_o = 5$ for $\phi = 0.001$–0.157.

with $\ell_b = e^2/4\pi\varepsilon_o\varepsilon kT$ the Bjerrum length, Q the number of charges per particle, and $a\kappa_o = (4\pi\ell_b \sum z_k^2 n_k)^{1/2}$ with z_k and n_k the valence and concentration of ions, in addition to the volume fraction. Numerical solutions to the Ornstein–Zernicke equation with a modified hypernetted chain closure via an existing computer code (Lionberger 1996) produced pair distribution functions (figure 4) at $a/l_b = 12.6$ ($a = 9$ nm), $Q = 75$, $a\kappa_o = 5$ and the full range of volume fractions for which the code convergences. Note the shift of the peak to smaller separations with increasing concentration due to crowding and increased screening. Figure 5 for $a\kappa_o = 5$ and $Q = 30$–900 demonstrates the dependence of $a\kappa$, the effective hard-sphere diameter $d_{eff}/2a$ (defined as the position of the first peak in $g(r)$) and the effective volume fraction $\phi_{eff} = \phi(d_{eff}/2a)^3$ on ϕ. The increase in the ionic strength and $a\kappa$ with volume fraction is quite significant, decreasing $d_{eff}/2a$ by as much as 20 % at the highest charge. Nonetheless, with $\phi \geqslant 0.30$ and $a\kappa \leqslant 5$ the effective volume fraction rises as high as 0.64 at the highest charge, thereby reaching well into the metastable fluid regime.

For adhesive hard spheres (Baxter 1968) with

$$\frac{\Phi}{kT}(s) = -\ln\frac{\delta(s-2)}{6\tau} s \geqslant 2, \tag{3.9}$$

the singular attraction that increases with $1/\tau$ is defined such that the second virial coefficient in the osmotic pressure takes the form $A_2 = 4 - 1/\tau$. Here we obtained the pair distribution function through an inverse fast Fourier transform of a closed-form solution for the static structure factor in the PY approximation (Regnaut & Ravey 1989),

$$\left.\begin{aligned} S^{-1}(\bar{q}) = {} & \left\{1 - \frac{3\phi}{2\bar{q}^3}\left[2A(2\bar{q}\cos 2\bar{q} - \sin 2\bar{q}) + B\bar{q}(\cos 2\bar{q} - 1) + \frac{\lambda\bar{q}^2}{3}\sin 2\bar{q}\right]\right\}^2 \\ & + \left\{\frac{3\phi}{2\bar{q}^3}\left[2A(2\bar{q}\sin 2\bar{q} + \cos 2\bar{q} - 1 - 2\bar{q}^2) + B\bar{q}(\sin 2\bar{q} - 2\bar{q})\right.\right. \\ & \left.\left. + \frac{\lambda\bar{q}^2}{3}(1 - \cos 2\bar{q})\right]\right\}^2 \\ A = {} & [1 + 2\phi - \lambda\phi(1-\phi)]/2(1-\phi)^2, \qquad B = -[3\phi - \lambda\phi(1-\phi)]/(1-\phi)^2, \end{aligned}\right\} \tag{3.10}$$

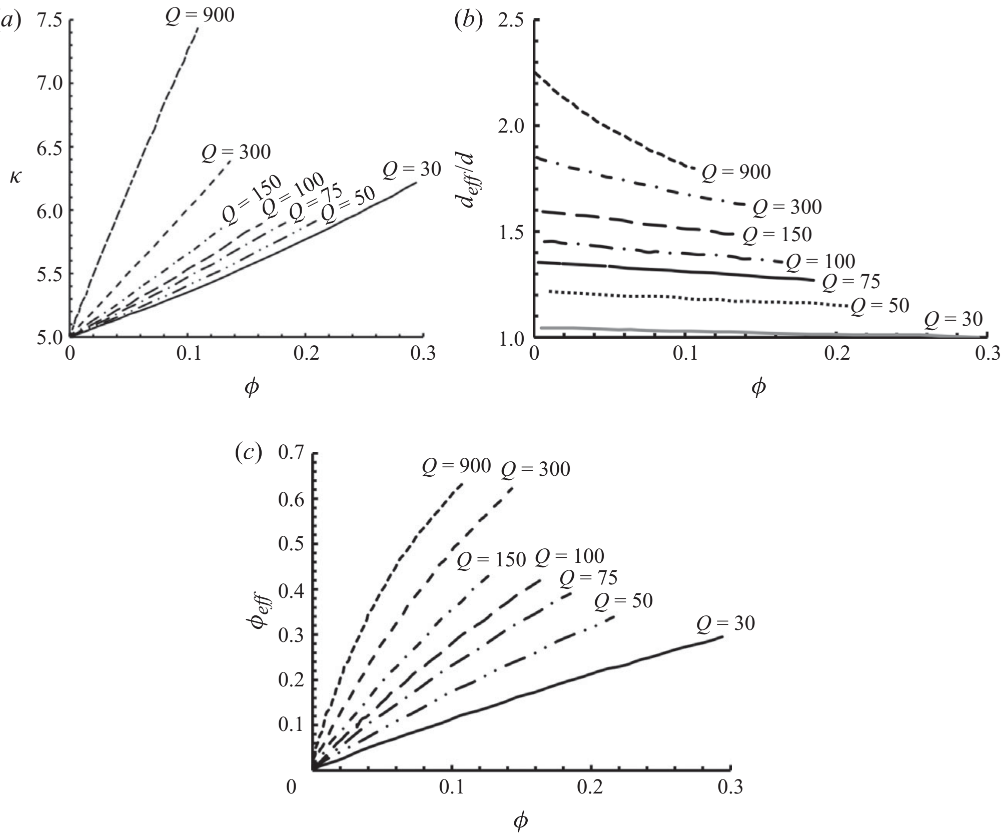

FIGURE 5. (*a*) Dimensionless screening length $a\kappa$, (*b*) effective hard-sphere diameter $d_{eff}/2a$, (*c*) and effective volume fraction ϕ_{eff}, for Yukawa potential with $a/\lambda_b = 12.6$, $a\kappa = 5$, $Q =$ 30–900.

with

$$\lambda = \frac{6}{\phi(1-\phi)}\left\{\phi + (1-\phi)\tau \pm \left[(\phi + (1-\phi)\tau)^2 - \frac{\phi}{3}\left(1 + \frac{1}{2}\phi\right)\right]^{1/2}\right\}, \quad (3.11)$$

and $\bar{q} = aq$, the wavenumber scaled on the particle radius. This strategy provides reasonable results (figure 6) for $\phi \geqslant 0.50$, which agree with those from Chiew & Glandt (1983). Note the delta function at contact with $\lim_{s\to 2} g(s) = \lambda/12\delta(s-2)$, which requires careful treatment in the inversion, the discontinuity at $r/2a = 2$, indicating strong binding to the second neighbour shell, and the discontinuity in slope at $r/2a = 4$.

The phase diagram for adhesive hard spheres (Rosenbaum *et al.* 1996) in figure 7 identifies an equilibrium fluid–solid transition, the metastable binodal with an associated spinodal, and the dynamic percolation and gelation boundaries (Seaton & Glandt 1987; Grant & Russel 1993). The pair distribution functions in figure 6 correspond to points in the non-percolated equilibrium fluid ($\phi = 0.10$ and 0.29, $\tau = 0.35$) and the non-percolated metastable fluid ($\phi = 0.10$ and 0.11), whereas the full calculations sampled $(\phi, \tau) = (0\text{–}0.40, 0.07\text{–}1.0)$, except the portion that lies within the spinodal where the theory fails. This includes points beyond the gelation boundary

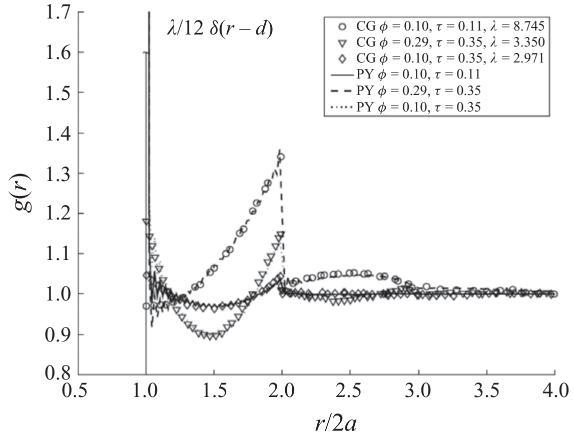

FIGURE 6. Pair distribution function for adhesive hard spheres from Percus–Yevick (lines) compared with results from Chiew & Glandt (1983) (symbols).

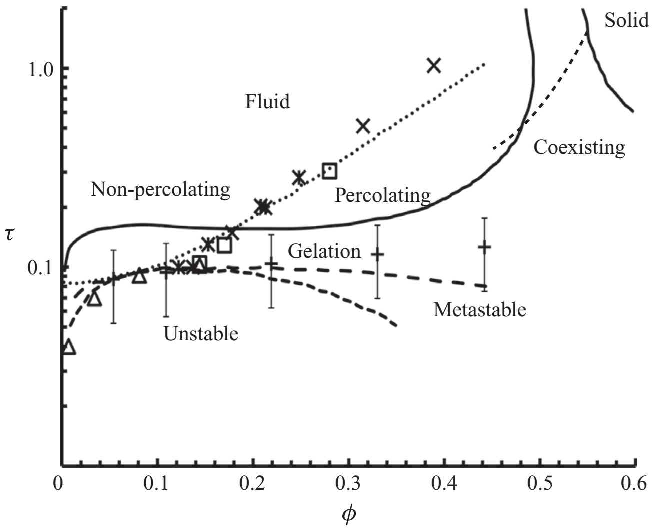

FIGURE 7. Phase diagram for adhesive hard spheres (Rosenbaum *et al.* 1996) indicating the fluid–solid transition ((- - -), the spinodal (△), the meta-stable binodal (– –) and the dynamic percolation transition (Chiew & Glandt 1983; Seaton & Glandt 1987) ····, ⋆, ×, □), and the gel line (+ +) from experiments (Grant & Russel 1993) (with permission).

as defined by the experimental points. The equilibrium fluid distribution function varies smoothly across the percolation transition and the gel transition, exhibiting no evidence of the dynamic long-range connectivity associated with the former or the localization responsible for the latter.

4. Bounds on the sedimentation velocity

As shown in the derivation of the upper bound, the rate of sedimentation depends upon the structure of the suspension through the first moment of the pair correlation function $h(r) = g(r) - 1$. In this section, the requisite integrations are performed to

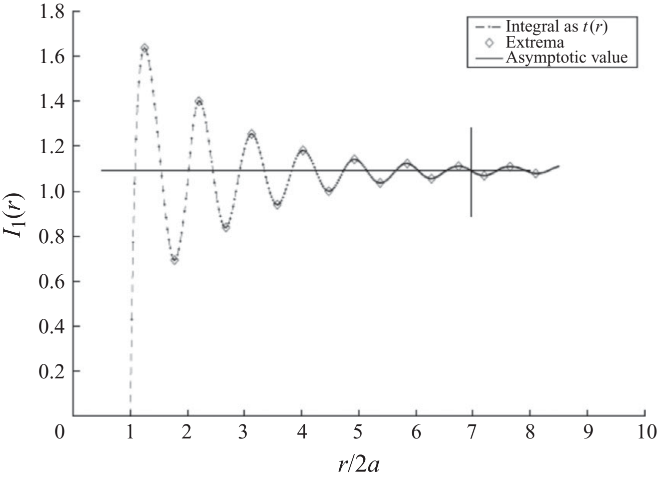

FIGURE 8. Computation of I_1 for hard spheres at $\phi = 0.60$ with vertical and horizontal lines indicating the average of two extrema, which coincides with the convergent $I_1(\infty)$.

determine the bounds for monodisperse dispersions of hard, charged and adhesive hard spheres as a function of volume fraction, which are then compared with data for model dispersions where available in the literature.

4.1. *Hard spheres*

The pair distribution function as depicted in figure 3 is zero within the excluded volume $0 < r/2a < 1$, which includes the physical volume of the sphere plus a shell of equal thickness into which a second hard sphere cannot penetrate. The probability jumps discontinuously at contact, generally to a value greater than unity due to interactions of the pair with other particles in a crowded dispersion. The nearest neighbour excludes other spheres, in turn producing a depleted layer farther out that generates the first of a series of decaying oscillations. These persist to large separations at high volume fractions, but the probability decays to unity at long distances, since the bulk dispersion is disordered.

Evaluation of the integral of the first moment, i.e.

$$I_1(r/2a) = \int_1^{r/2a} sh(s)\,\mathrm{d}s, \tag{4.1}$$

acquires much of its ultimate value within the first shell but at high concentrations takes many oscillations to settle into the final, asymptotic value, as illustrated in figure 8. Fortunately, the midpoints of the oscillations become predictive of the final asymptote well before the oscillations decay completely as illustrated in the figure. One striking observation (Gilleland 2004) is that distribution functions from Percus–Yevick, Percus–Yevick corrected by Verlet–Weis, and MC simulations produce essentially the same value for $I_1(\infty)$, despite significant differences in the contact value and decay rate. Figure 9 illustrates this for the latter two distributions. A small discrepancy between Verlet–Weis and Monte Carlo for $\phi > 0.55$, i.e. within the metastable fluid region, may arise from the different shape in the second neighbour shell, where the MC results exhibit a stronger split peak with less area under the curve. Nonetheless, the difference falls within the uncertainty of the MC simulations and the extrapolation of the VW correction.

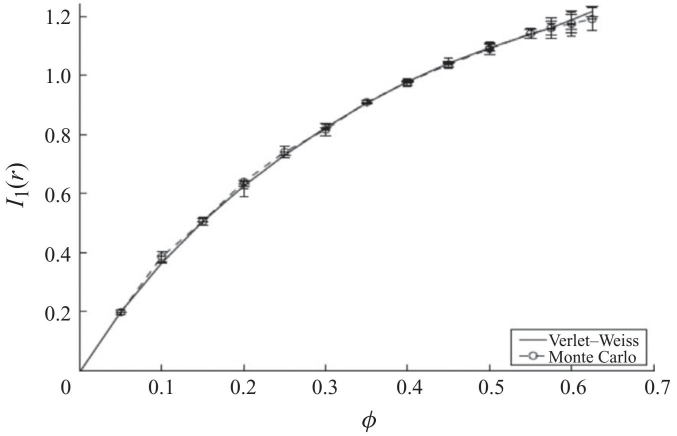

FIGURE 9. Results for $I_1(\infty)$ from VW (—) and MC (–○–) distributions with error bars for simulations.

The results for the upper bound on U/U_o from both distributions are compared in figure 10 with published data from several different hard-sphere dispersions: polystyrene/water (Buscall *et al.* 1982), silica/cyclohexane (de Kruif *et al.* 1987), PMMA/decalin (Paulin & Ackerson 1990) and silica/ethylene glycol (Xue *et al.* 1992). The fact that $I_1(\infty) > 0$ for hard spheres reflects the excess of nearest neighbours, which compensates in part for the -5ϕ retardation of the sedimentation velocity in (2.31) due to backflow in the excluded shell. Thus, the upper bound lies well above the dilute limit of $U/U_o = 1–6.55\phi$. The graph confirms that the available experimental data are bounded from above by the upper bounds derived here, fairly tightly at the dilute end but quite loosely at the concentrated end.

The line correlating the data in figure 10,

$$U/U_o = (1-\phi)^{5.4}, \tag{4.2}$$

appears in figure 11 for comparison with other theoretical results. Note that the new upper bounds are much closer to the data than Luke's (1992, 1993) earlier version. The theory of Brady & Durlofsky (1988) cited above falls closer to the data beyond the dilute limit where the two coincide according to (1.6). Lastly, the figure includes an upper bound calculated with additional terms in the velocity fields that yield no force or torque on the particles but reduce the dissipation (Beasley & Torquato 1989). These do in fact bring the bound closer to the data, but only by a small amount for $\phi > 0.40$.

In conclusion, our evaluation of an upper bound on sedimentation velocity for hard spheres is sensitive to the structure of the equilibrium pair correlation function, but not particularly sensitive to the details. This provides a sound basis for investigating the effect of other interparticle potentials, which are known to affect profoundly the sedimentation velocity.

4.2. *Charged spheres*

For charged spheres the pair distribution function resembles that of hard spheres but with a larger excluded volume due to the electrostatic repulsion, as reflected in the larger effective diameter $d_{eff} > 2a$ and larger effective volume fraction $\phi_{eff} > \phi$. This additional excluded volume translates into a quite negative first moment of the pair distribution $I_1(\infty)$ for $\phi < 0.15$, as illustrated in figure 12 for $a/\lambda_b = 12.6$ ($a = 9$ nm),

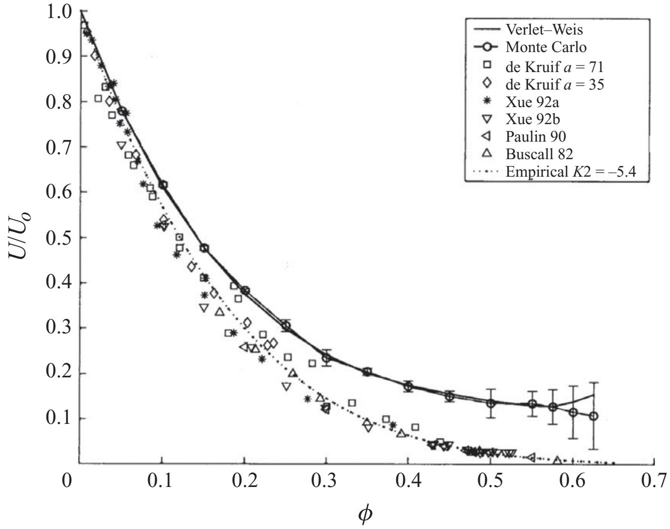

FIGURE 10. Upper bound on sedimentation velocity for hard spheres compared with data (Jansen *et al.* 1986; Buscall *et al.* 1982; Paulin & Ackerson 1990; Xue *et al.* 1992) and the resulting correlation (· · • · ·).

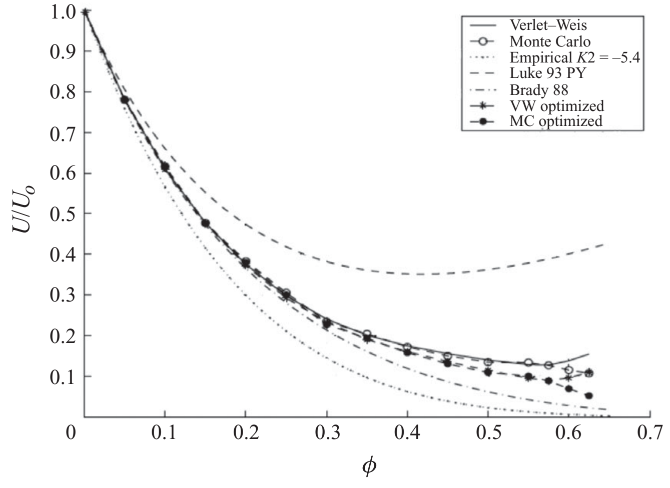

FIGURE 11. Normalized sedimentation velocity for hard spheres as a function of volume fraction from Verlet-Weis and Monte Carlo distributions compared with the correlation, theory (Brady & Durlofsky 1988), and Luke's (1993) upper bound.

$a\kappa_o = 5$ and $Q = 30$–900. Note that the much larger excluded volume masks the small amplitude oscillations evident for hard spheres. At higher volume fractions, many-body interactions force the particles closer together and $I_1(\infty)$ asymptotes to that for hard spheres or $Q = 0$.

Substitution of the set of $I_1(\infty)$ into (2.31) produces upper bounds in figure 13 that tend towards the bound for hard spheres (-○-) at high volume fractions and lower charges and approach the sedimentation velocity expected for a face-centred cubic array (-●-) for larger charge densities and volume fractions. Note that the calculation of the face-centred cubic array accounts fully for hydrodynamic interactions, so our

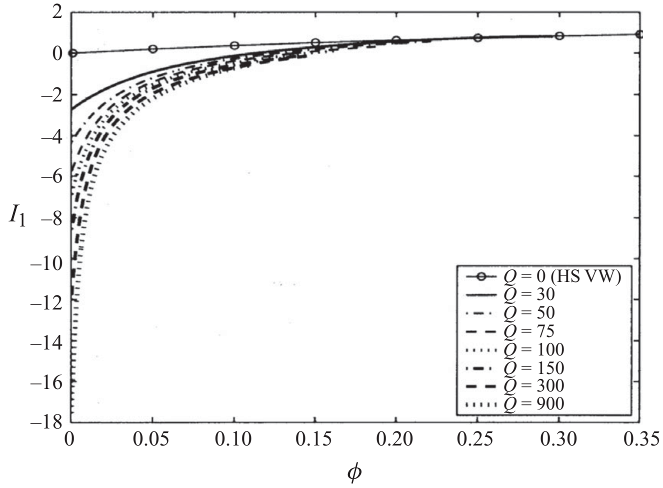

FIGURE 12. Results for $I_1(\infty)$ for charged spheres as a function of ϕ for $a/\lambda_b = 12.6$, $a\kappa_o = 5$ and $Q = 0$–900.

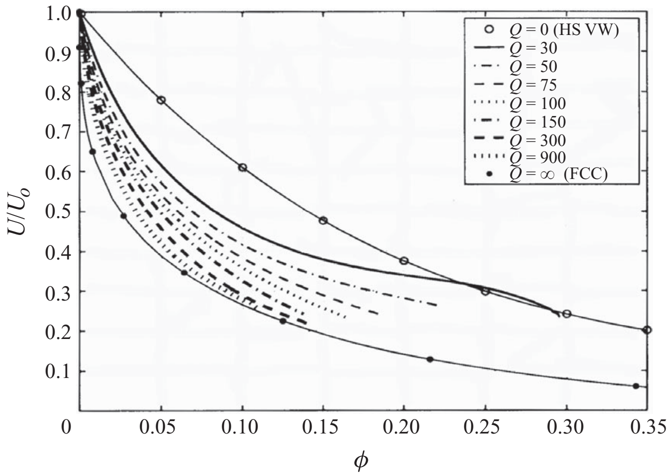

FIGURE 13. Sedimentation velocity for charged spheres as a function of volume fraction for $Q = 30$–900 at $a\kappa_o = 5$ and $a/\lambda_b = 12.6$ compared with hard spheres (○) and a face-centred cubic array (●), which might be considered $Q = \infty$.

result should be an upper bound for that limit even though the structure does not approach the face-centred cubic. The second plot of results in figure 14 reinforces this with bounds for $a/\lambda_b = 12.6$, $Q = 100$ and $a\kappa_o = 1$–25. Note that the curves for $a\kappa_o = 1$ and 2 merge with the face-centred cubic curve as the effective volume fraction becomes volume-filling. In both figures the uppermost bound strays slightly above the hard-sphere limits, probably reflecting inconsistencies in the thermodynamic approximations for the pair distribution functions.

Figure 15 compares the bounds with sedimentation velocities measured by Klein and coworkers (Thies-Weesie *et al.* 1995) for silica spheres ($a = 386$ nm) in ethanol at a range of ionic strengths corresponding to $a\kappa_o = 0$–19, based on the added electrolyte. Given the considerable difference in particles size from our calculations, the only feasible comparison is at $a\kappa_o = 5$ for their experiment with $Q = 350$ and $a = 386$ nm

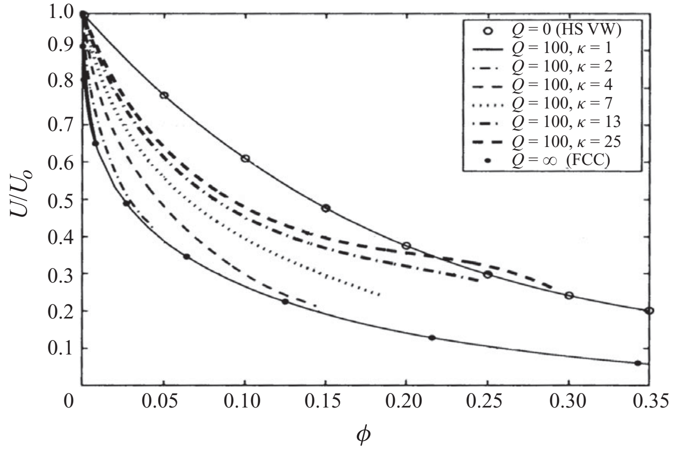

FIGURE 14. Sedimentation velocity for charged spheres as a function of volume fraction for $a/\lambda_b = 12.6$ and $Q = 100$ at $a\kappa_o = 1$–25 compared with hard spheres (○) and a face-centred cubic array (●).

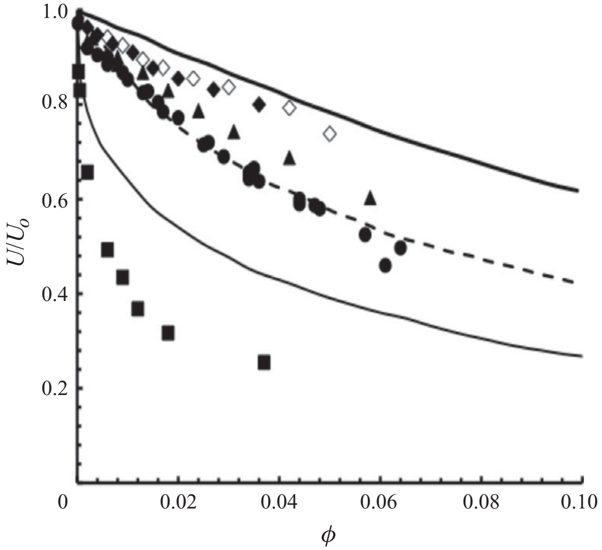

FIGURE 15. Data from Thies–Weesie *et al.* (1995) for silica dispersions in ethanol with $a\kappa_o = 0$ (■), 5 (●), 10 (▲) and 19 (◆, ◇) with $a/\lambda_b = 541$ and $Q = 350$ (assumed), compared with upper bounds for $a/\lambda_b = 12.6$, $a\kappa_o = 5$ and $Q = \infty$ (—), 50 (- - -), 0 (**—**) from bottom to top.

and our bound for $Q = 50$ and $a = 9$ nm. In this case, the prefactor in the Yukawa potential (3.7) for our upper bound $(\lambda_b/a)Q^2 = (0.714/9) \times 50^2 = 198$ is close to that for their experiment $(0.714/386) \times 350^2 = 227$, though the sensitivity of the ionic strength to volume fraction (3.8) differs somewhat due the dependence on $(\lambda_b/a)Q$. The bound is almost coincident with the data, providing some support for the theory.

4.3. *Adhesive hard spheres*

The graphs in figure 16 reveal the cumulative integral I_1 for adhesive hard spheres to be positive with a step change at contact due to clustering produced by the singular attraction and a steady increase with separation for several additional shells before

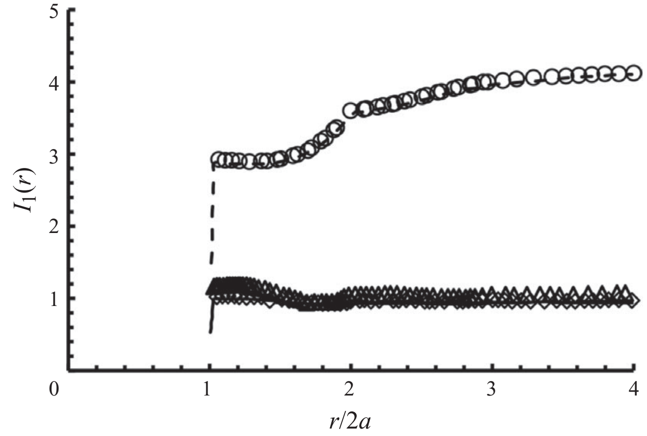

FIGURE 16. Calculations of I_1 from the PY distribution for adhesive hard spheres compared to results from Chiew & Glandt (1983) for three sets of conditions.

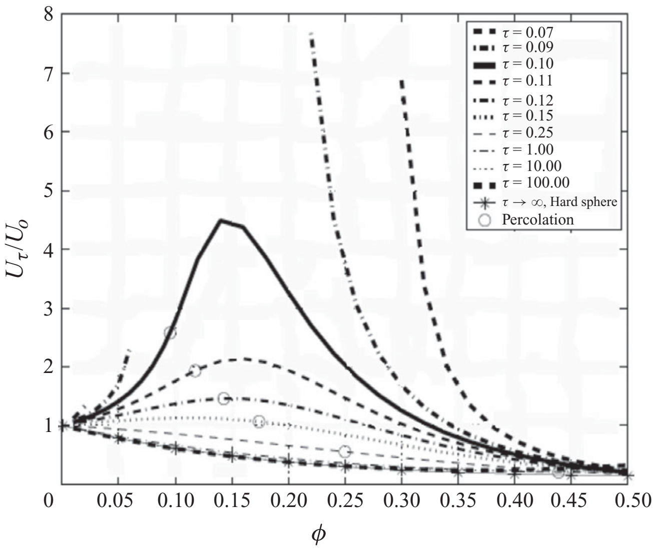

FIGURE 17. The upper bound on the sedimentation velocity for adhesive hard spheres for $\tau = 0.07$, 0.09, 0.10, 0.11, 0.12, 0.15, 0.25, 1.0 and 100 (hard spheres) from top to bottom with the percolation transition noted (○).

converging. The magnitude of the step function approximates the integral over the delta function and is proportional to $1/\tau$. The positive sign for I_1 indicates that clustering in the accessible volume, i.e. $r > 2a$, dominates any short-range depletion. Though not shown, I_1 increases with volume fraction from infinite dilution to about $\phi = 0.15$ and then decreases monotonically as packing considerations disrupt the delicate network set up by the adhesive contacts (Gilleland 2004). The integral eventually converges with the positive hard-sphere limit as the structure becomes homogeneous at higher concentrations.

The corresponding results for the upper bound on sedimentation of adhesive spheres presented in figure 17 for $\tau = 0.07$–100 are bounded from below by the hard-sphere result corresponding to $\tau = \infty$. Gaps in the curves for $\tau = 0.07$ and 0.09

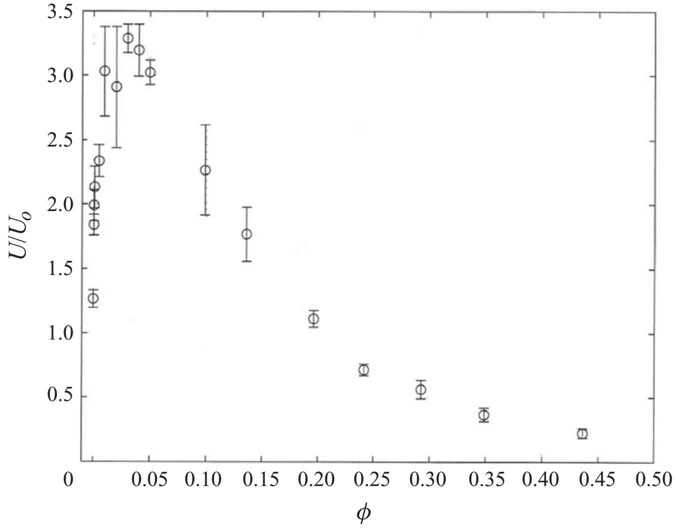

FIGURE 18. Experimental data reproduced from Bickert & Stahl (1996) for adhesive hard spheres of unknown τ.

reflect inaccessible points within the spinodal, where the PY theory breaks down, and the circles indicate the dynamic percolation transition (Seaton & Glandt 1987). The bound increases dramatically with the adhesive strength at intermediate volume fractions with a maximum in the vicinity of the critical point. Beyond that the increasingly homogeneous packing brings the bound down, presumably to eventually converge with that for hard spheres.

While rapid sedimentation for flocculated dispersions has been known and exploited technologically for many decades, quantitative measurements of rates over a full range of volume fraction are rare. One of the few examples, albeit without a measure of the strength of the attraction, is depicted in figure 18 (Bickert & Stahl 1996). Note the rapid increase at low concentrations, suggesting a dilute limit of $U/U_o = 1 + 100\phi$ and, therefore, $1/\tau \sim 50$. The shape of the curve departs significantly from the upper bounds in figure 17 for equilibrium, albeit metastable, fluids. This may reflect a consequence of the gel transition, which imposes a solid-like structure that resists gravity and slows sedimentation dramatically (Buscall & White 1987). This, of course, falls outside of the scope of the upper bounds calculated here and, therefore, limits their applicability.

5. Conclusions

The upper bounds on the sedimentation velocity presented here illustrate both the sensitivity of this transport property to the thermodynamic state of the dispersion and the power of bounds based on relatively crude approximations to the hydrodynamics. Of course, the sedimentation velocity, like the mutual diffusion coefficient, is most sensitive to collective motion of nearest neighbours, unlike the shear viscosity and self-diffusion coefficient that require relative motion. The bound constructed here clearly surpasses that published earlier by Luke but is far from the most accurate that might be constructed. To tighten the bound, however, would require tedious evaluation of higher-dimension integrals and higher-order correlation functions only accessible through simulations. In the meantime, the bound supports the application of the formula from Brady & Durlofsky (1988) for dispersions beyond hard spheres, with either attractive or longer range repulsive interactions, thereby providing confidence in estimating sedimentation velocities for systems that have yet to attract the attention of Stokesian dynamics or other simulations.

S.T. was supported by the Office of Basic Energy Sciences, US Department of Energy, grant DE-FG02-04-ER46108. W.T.G. and W.B.R. were supported by the Chemical and Thermal Systems, Division of Engineering, National Science Foundation, grant CTS 9521662.

REFERENCES

Allen, M. P. & Tildesley, D. J. 1987 *Computer Simulation of Liquids*. Clarendon Press.

Batchelor, G. K. 1972 Sedimentation in a dilute dispersion of spheres. *J. Fluid Mech.* **52**, 245–268.

Baxter, R. J. 1968 Percus–Yevick equation for hard spheres with surface adhesion. *J. Chem. Phys.* **49**, 2770–2774.

Baxter, R. J. 1970 Orstein–Zernicke relation and Percus–Yevick approximation for fluid mixtures. *J. Chem. Phys.* **52**, 4559–4562.

Beasley, J. D. & Torquato, S. 1989 New bounds on the permeability of a random array of spheres. *Phys. Fluids* A **1**, 199–207.

Bickert, G. & Stahl, W. 1996 Sedimentation behavior of mono- and polydisperse submicron particles in dilute and in concentrated suspensions. In *7th World Filtration Conference, Budapest, Hungary*.

Brady, J. F. & Durlofsky, L. J. 1988 The sedimentation rate of disordered suspensions. *Phys. Fluids* **31**, 717–727.

Buscall, R., Goodwin, J. W., Ottewill, R. H. & Tadros, T. F. 1982 The settling of particles through Newtonian and non-Newtonian media. *J. Colloid Interface Sci.* **85**, 78–86.

Buscall, R. & White, L. R. 1987 The consolidation of concentrated suspensions. *J. Chem. Soc. Faraday Trans.* I **83**, 873–891.

Chiew, Y. C. & Glandt, E. D. 1983 Percolation behavior of permeable and adhesive spheres. *J. Phys.* A*: Math. Gen.* **16**, 2599–2608.

Clarke, A. S. & Wiley, J. D. 1987 Numerical simulation of the dense random packing of a binary mixture of hard spheres: amorphous metals. *Phys. Rev.* B **35**, 7350–7356.

Fleer, G. J., Cohen Stuart, M. A., Scheutjens, M. H. M., Cosgrove, T. & Vincent, B. 1993 *Polymers at Interfaces*. Chapman and Hall.

Gilleland, W. T. 2004 New bounds to estimate the sedimentation velocities or monodispers and binary colloidal suspensions. PhD thesis, Princeton University, Princeton, NJ.

Grant, M. C. & Russel, W. B. 1993 Volume-fraction dependence of elastic moduli and transition temperatures for colloidal silica gels. *Phys. Rev.* E **47**, 2606–2614.

Hansen, J.-P. & McDonald, I. R. 1986 *Theory of Simple Liquids*. Academic Press.

Hunter, R. J. 1987 *Foundations of Colloid Science*. Oxford University Press.

Jansen, J. W., de Kruif, C. G. & Vrij, A. 1986 Attractions in sterically stabilized silica dispersions. Part IV. Sedimentation. *J. Colloid Interface Sci.* **114**, 501–504.

de Kruif, C. G., Jansen, J. W. & Vrij, A. 1987 A sterically stabilized silica colloid as a model supramolecular fluid. In *Physics of Complex and Supramolecular Fluids*. Wiley Interscience.

Lionberger, R. A. 1996 Rheology, structure and diffusion in concentrated colloidal dispersions. PhD thesis, Princeton University, Princeton, NJ.

Luke, J. H. C. 1992 A minimum principle for Stokes flows containing rigid particles and an upper bound on the sedimentation speed. *Phys. Fluids* A **4**, 212–219.

Luke, J. H. C. 1993 A variational upper bound on the renormalized mean sedimentation speed in concentrated suspensions of identical randomly arranged spheres. *SIAM J. Appl. Math.* **53**, 1613–1635.

Moncha-Jorda, A., Louis, A. A. & Padding, J. T. 2010 Effects of interparticle attractions on colloidal sedimentation. *Phys. Rev. Lett.* **104**, 068301 (1–4).

Napper, D. H. 1983 *Polymeric Stabilization of Colloidal Dispersions*. Academic Press.

Nguyen, N. Q. & Ladd, A. J. C. 2005 Sedimentation of hard-sphere suspensions at low Reynolds number. *J. Fluid Mech.* **525**, 73–104.

O'Brien, R. W. 1979 A method for the calculation of the effective transport properties of suspensions of interacting particles. *J. Fluid Mech.* **91**, 17–39.

Paulin, S. E. & Ackerson, B. J. 1990 Observation of a phase transition in the sedimentation velocity of hard spheres. *Phys. Rev. Lett.* **64**, 2663–2666.

Pusey, P. N. 1991 *Liquides, Cristallisation et Transition Vitreuse*. Elsevier Science.

Regnaut, C. & Ravey, J. C. 1989 Application of the adhesive sphere model to the structure of colloidal suspensions. *J. Chem. Phys.* **91**, 1211–1221.

Rintoul, M. D. & Torquato, S. 1996 Computer simulations of dense hard-sphere systems. *J. Chem. Phys.* **105**, 9258–9265.

Rintoul, M. D. & Torquato, S. 1998 Hard-sphere statistics along the metastable amorphous branch. *Phys. Rev.* E **58**, 532–537.

Rosenbaum, D., Zamora, P. C. & Zukoski, C. F. 1996 Phase behavior of small attractive colloidal particles. *Phys. Rev. Lett.* **76**, 150–153.

Russel, W. B., Saville, D. A. & Schowalter, W. R. 1991 *Colloidal Dispersions*. Cambridge University Press.

Seaton, N. A. & Glandt, E. D. 1987 Aggregation and percolation in a system of adhesive spheres. *J. Chem. Phys.* **86**, 4668–4677.

Steinhardt, P. J., Nelson, D. R. & Ronchetti, M. 1983 Bond-orientational order in liquids and glasses. *Phys. Rev.* B **28**, 784–805.

Thies-Weesie, D. M. E., Philipse, A. P., Nagele, G., Mandl, B. & Klein, R. 1995 Nonanalytic concentration dependence of sedimentation of charged spheres in an organic solvent: experiments and calculations. *J. Colloid Interface Sci.* **176**, 43–54.

Torquato, S. 2002 *Random Heterogeneous Materials: Microstructure and Macroscopic Properties*. Springer.

Torquato, S. & Beasley, J. D. 1987 Bounds on the permeabiity of a random array of partially penetrable spheres. *Phys. Fluids* **30**, 633–641.

van de Ven, T. G. M. 1989 *Colloidal Hydrodynamics*. Academic Press.

Verlet, L. & Weis, J.-J. 1972 Equilibrium theory of simple liquids. *Phys. Rev.* A **5**, 939–952.

Xue, J. Z., Herbolzheimer, E., Rutgers, M. A., Russel, W. B. & Chaikin, P. M. 1992 Diffusion, dispersion, and settling of hard spheres. *Phys. Rev. Lett.* **69**, 1715–1718.

Zick, A. A. & Homsy, G. M. 1982 Stokes flows through periodic arrays of spheres. *J. Fluid Mech.* **115**, 13–26.